Research Square

Preprints are preliminary reports that have not undergone peer review.
They should not be considered conclusive, used to inform clinical practice,
or referenced by the media as validated information.

Prediction of Neoadjuvant Therapy Response in Locally Advanced Gastric Cancer Based on ctSLEP Score and Spectral CT

Yue Peng
Lanzhou University
Xuan Guo
Lanzhou University
Tiezhu Ren
Lanzhou University
Qianqian Chen
Lanzhou University
Long Ma
Lanzhou University
Wenjuan Zhang
hxzhangwj121@163.com
Lanzhou University

Research Article

Keywords: Stomach, Gastric cancer, Spectral computed tomography, Neoadjuvant therapy, Treatment response

Posted Date: June 2nd, 2026

DOI: https://doi.org/10.21203/rs.3.rs-9526851/v1

License: This work is licensed under a Creative Commons Attribution 4.0 International License.
Read Full License

Additional Declarations: No competing interests reported.

Abstract

Background

To develop and validate a novel, noninvasive CT-based invasion score (ctSLEP), integrating serosal invasion, lymphovascular invasion, extramural vascular invasion, and occult peritoneal metastasis, combined with spectral CT parameters, for preoperative prediction of neoadjuvant therapy response in locally advanced gastric cancer.

Methods

In this retrospective study, patients with locally advanced gastric cancer undergoing neoadjuvant therapy followed by surgery (November 2020–November 2025) were included. The ctSLEP score was constructed from CT-detected tumor invasion features. Spectral CT parameters and clinical variables were analyzed. Tumor regression grade by Becker criteria served as the reference standard. Multivariable logistic regression was applied to develop predictive models in training (70%) and validation (30%) cohorts.

Results

A total of 158 patients (mean age, 57.35 ± 7.89 years; 126 men) were evaluated; 65/158 (41.1%) were responders. Independent predictors of response included neutrophil-to-lymphocyte ratio (OR = 1.680; 95% CI: 1.160–2.567; $p = 0.01$), iodine concentration in the venous phase (OR = 0.853; 95% CI: 0.731–0.987; $p = 0.04$), arterial enhancement fraction (OR = 0.195; 95% CI: 0.044–0.812; $p = 0.03$), and components of the ctSLEP score: extramural vascular invasion ($p < 0.001$), occult peritoneal metastasis ($p = 0.03$), and lymphovascular invasion ($p = 0.02$). The final model incorporating ctSLEP achieved an AUC of 0.880.

Conclusions

The ctSLEP score, combined with spectral CT parameters and inflammatory markers, may provide a noninvasive tool for preoperative risk stratification and treatment-response prediction in patients with locally advanced gastric cancer.

Key Points

A CT-based invasion score integrating four morphological features captures tumor aggressiveness.

Combining this score with spectral CT parameters enables accurate prediction of neoadjuvant therapy response.

The multiparametric model also stratifies relapse risk, supporting individualized prognosis.

Clinical Relevance Statement

The ctSLEP score provides a noninvasive, clinically actionable tool to identify biologically aggressive tumors and patients at high risk of poor response or relapse, supporting individualized preoperative treatment planning.

Introduction

Gastric cancer (GC) is the fifth most common and lethal malignancy globally, with over 50% of patients diagnosed at the locally advanced gastric cancer (LAGC) stage, where the five-year survival rate remains below 30%[1, 2]. Neoadjuvant therapy (NAT) has become the standard treatment for LAGC, significantly improving prognosis when followed by surgery compared to surgery alone[3–5]. However, the efficacy of NAT varies considerably among individuals, with approximately 50% of patients showing inadequate response, potentially leading to unnecessary side effects[6]. Therefore, accurately identifying patients who are likely to benefit from NAT prior to surgery is crucial for optimizing treatment strategies. Currently, Tumor regression grade (TRG) is the gold standard for assessing pathological responses to NAT[7]. However, TRG is invasive and provides delayed results, necessitating the development of non-invasive and timely methods for evaluating treatment efficacy.

During GC progression, several key pathological features contribute to local invasion and distant spread, including serosal invasion (SI), lymphovascular invasion (LVI), extramural vascular invasion (EMVI), and peritoneal metastasis (PM) [8–12]. SI refers to tumor penetration beyond the serosal layer, conferring potential for intraperitoneal spread, while PM indicates the presence of established peritoneal seeding. LVI and EMVI reflect tumor cell dissemination through lymphatic and hematogenous routes, respectively. These features are closely associated with poor prognosis and may influence tumor responsiveness to NAT. Recent CT-based imaging assessment systems, such as CT detected EMVI (ctEMVI), LVI (ctLVI), and occult peritoneal metastasis (ctOPM), have proven valuable in GC prognosis[13]. However, the relationship between these morphological features and NAT efficacy remains to be further explored.

Spectral CT provides quantitative parameters, such as iodine concentration (IC), arterial enhancement fraction (AEF), and extracellular volume fraction (ECV), which reflect tumor angiogenesis and microenvironmental heterogeneity[14–16]. Additionally, these parameters have shown significant potential for evaluating treatment response and predicting LVI and PM[17–20]. However, existing studies have primarily focused on combining spectral CT with clinicopathological factors, with limited exploration of integrating spectral CT quantitative data with morphological imaging scores. In addition to spectral CT parameters, systemic inflammatory markers have also been linked to NAT response, yet their combined utility with imaging scores remains unclear.

Therefore, this study integrates CT-detected invasion features (ctSI, ctLVI, ctEMVI and ctOPM) to develop a comprehensive CT-based invasion score (ctSLEP). We also combine multi-parametric spectral CT indices and clinical factors to create a non-invasive model for predicting NAT response in LAGC patients, highlighting the incremental value of ctSLEP beyond spectral CT and inflammatory biomarkers for individualized preoperative decision-making.

Materials and Methods

Study Design and Population

This was a retrospective study conducted at the Second Hospital of Lanzhou University. Patients with gastric cancer who underwent CT examination were retrospectively reviewed. Relevant clinical and imaging data were collected and analyzed anonymously. Patients with LAGC who received NAT between November 2020 and November 2025 were screened. All patients underwent triphasic contrast-enhanced spectral CT examinations before treatment. Detailed CT acquisition protocols are provided in **Supplementary Table S1**.

Inclusion criteria were as follows: (1) LAGC staged as cT2–4aN0–3M0 according to the UICC/AJCC 8th edition, with postoperative pathological confirmation of gastric adenocarcinoma (**Supplementary Table S2**) ; (2) completion of NAT followed by radical gastrectomy with D2 lymphadenectomy; (3) availability of high-quality spectral CT images suitable for analysis; and (4) complete postoperative tumor regression grading (TRG) assessed according to Becker's criteria. Exclusion criteria included missing key clinical, pathological, or imaging data; a history of other malignancies; or inability to assess peritoneal status, including definite CT signs of peritoneal metastasis.

Ultimately, 158 patients with LAGC were included **(**Fig. 1). Additionally, clinical, pathological characteristics and NAT regimens were collected from the medical records, as described in **Supplementary Appendices 1 and 2**.

Post-processing and CT Image Analysis

Raw spectral CT images acquired using the Revolution Spectral CT system were transferred to an ADW 4.7 workstation (GE Healthcare) for post-processing and analysis with the spectral scan viewer software. Two radiologists with 2 and > 5 years of experience in abdominal imaging independently performed region-of-interest (ROI) delineation and quantitative analysis. Both readers were blinded to clinical data and postoperative pathological results. Discrepancies were resolved by consensus.

For each lesion, measurements were performed independently three times by each radiologist, and the averaged values were used for subsequent analyses. On iodine-based images obtained in the arterial, venous, and delayed phases (AP, VP, and DP), the largest axial slice of the tumor and the adjacent superior and inferior slices were selected. Circular or elliptical ROIs were manually drawn to cover

approximately 2/3 of the tumor area, while avoiding visible vessels, necrosis, hemorrhage, and calcification.

The following parameters were recorded: CT values on monoenergetic images at 40 keV (CT_{40}keV) and 70 keV (CT_{70}keV), iodine concentration (IC) of the lesion, and iodine concentration of the abdominal aorta at the corresponding slice level (IC□□). Based on these measurements, quantitative indices were calculated as follows: normalized iodine concentration (nIC = IC / IC□□); spectral attenuation curve slope (λHU = [CT_{40}keV − CT_{70}keV] / 30); extracellular volume fraction (ECV = [1 − HCT] × [ICDP / IC□□DP] × 100%); and arterial enhancement fraction (AEF = ICAP / ICDP). Detailed measurement procedures, definitions and illustration images of spectral CT–derived parameters are provided in the **Supplementary Table S3** and **Supplementary Figure S1**.

Construction of CT Sign–Integrated Scoring System

By adjusting the window width and window level, tumors were more precisely localized and their ctSI, ctEMVI, ctOPM, and ctLVI features were comprehensively evaluated on contrast-enhanced images in the axial, coronal, and sagittal planes. This study integrated the ctSI findings into the scoring system proposed by Li et al.[13],which included ctEMVI, ctLVI, and ctOPM. Furthermore, by integrating these four invasive imaging features, we developed a novel composite imaging score. Detailed scoring criteria and representative illustrations are provided in Fig. 2 **and Supplementary Appendix 3**.

Clinical endpoints

The primary outcome of this study was TRG response, with recurrence-free survival (RFS) as the secondary outcome. For definitions of endpoints, please refer to **Supplementary Appendix 4**.

Statistical analysis

All statistical analyses were performed using R software (version 4.5.1). Normality of continuous variables was assessed with the Kolmogorov–Smirnov test. Normally distributed variables are reported as mean ± standard deviation (SD), whereas non-normally distributed variables are presented as median (interquartile range [IQR], 25th–75th percentiles). Categorical variables are summarized as counts and percentages and were compared using the χ^2 test or Fisher's exact test, as appropriate. Intraobserver and interobserver agreement analyses were performed for the assessments of the two radiologists (**Supplementary Appendix 5**). Multicollinearity among covariates was examined using the variance inflation factor (VIF); variables with VIF > 5 were excluded from subsequent analyses.

Associations between candidate predictors and response to NAT were investigated using multivariable logistic regression. Subsequently, the cohort was randomly split into a training set (70%) and a validation set (30%) to develop and evaluate the predictive models. Eight candidate models were developed based on the four invasive imaging features using different feature-combination strategies: (i) entering the four

features simultaneously; (ii) a simple additive composite score (sum of the four features); (iii) a principal component analysis (PCA)–derived composite retaining components explaining > 80% of the variance(**Supplementary Table S4a-4b**); and (iv) a cross-validated weighted composite score, where the weighting coefficients are derived from the β estimates obtained through five-fold cross-validation, and applied to generate new indices (a total of eight models were co-generated through corresponding model variants).

The optimal model was selected according to overall performance. Shapley Additive Explanations (SHAP) were used to quantify and visualize feature importance in the selected model(**Supplementary Figure S2**), and a nomogram was constructed for individualized prediction.

After confirming the proportional hazards assumption, Cox proportional hazards regression was performed to assess associations between covariates and the risk of recurrence or metastasis. Relapse-free survival was additionally compared across groups using Kaplan–Meier curves and the log-rank test.

Results

Comparison of baseline characteristics between the NAT response group and the no-response group

A total of 158 patients with LAGC were included (men/women, 126/32; mean age, 57.35 ± 7.89 years). Pathologic response to NAT was evaluated using the Becker TRG system. Overall, 65 patients (41.1%) were classified as responders (TRG 1a/1b) and 93 (58.9%) as non-responders (TRG 2/3). Responders had a significantly lower neutrophil-to-lymphocyte ratio (NLR) than non-responders (2.20 (1.76, 2.92) vs 2.62 (1.94, 3.87); $p = 0.006$). On spectral computed tomography (CT), responders showed higher ICAP (14.47 (12.75, 19.54) vs 12.14 (9.51, 14.74); $p < 0.001$), nICAP (0.12 (0.09, 0.15) vs 0.10 (0.07, 0.13); $p < 0.001$), ICVP (18.00 (15.41, 21.73) vs 15.86 (13.86, 18.34); $p = 0.002$), nICVP (0.45 (0.37, 0.58) vs 0.39 (0.35, 0.47); $p = 0.008$), and higher AEF(1.00 (0.80, 1.17) vs 0.77 (0.61, 0.86); $p < 0.001$). Non-responders had higher positivity rates of ctSI, ctEMVI, ctOPM and ctLVI (all $p < 0.05$), whereas other clinicopathologic and imaging variables did not differ significantly (all $p > 0.05$) (Table 1a-1b). Both intra- and inter-observer agreements were good to excellent across parameters(**Supplementary Table S5**).

Table 1a
Comparison of baseline clinicopathological characteristics between the NAT response group and the no-response group

Variables	Overall (n = 158)	Responders (TRG = 1a/1b, n = 65)	Non-responders (TRG = 2 / 3, n = 93)	χ2/t/Z value	*P* value
Age	57.35 ± 7.89	57.34 ± 7.91	57.35 ± 7.91	-0.01	0.99
NLR	2.40 (1.85, 3.49)	2.20 (1.76, 2.92)	2.62 (1.94, 3.87)	-2.73	0.006
LMR	3.52 (2.50, 4.88)	3.75 (3.19, 5.18)	3.37 (2.30, 4.57)	-1.93	0.05
BMI	22.17 (20.05, 24.35)	21.91 (19.72, 23.88)	22.31 (20.38, 25.14)	-1.23	0.22
Gender				0.11	0.74
Female	32 (20.25)	14 (21.54)	18 (19.35)		
Male	126 (79.75)	51 (78.46)	75 (80.65)		
Location				-	0.06
Cardia/Fundus	44 (27.85)	12 (18.46)	32 (34.41)		
Body	45 (28.48)	19 (29.23)	26 (27.96)		
Antrum/Pylorus	61 (38.61)	32 (49.23)	29 (31.18)		
Diffuse	8 (5.06)	2 (3.08)	6 (6.45)		
Borrman				4.73	0.09
I	15 (9.49)	10 (15.38)	5 (5.38)		
II/III	122 (77.22)	48 (73.85)	74 (79.57)		
IV	21 (13.29)	7 (10.77)	14 (15.05)		
Differentiation				0.14	0.71
Well/Moderate	66 (41.77)	26 (40.00)	40 (43.01)		
Poor	92 (58.23)	39 (60.00)	53 (56.99)		
NAT method				0.12	0.73
NAC	51 (32.28)	20 (30.77)	31 (33.33)		
NAC combined	107 (67.72)	45 (69.23)	62 (66.67)		

NAC: Neoadjuvant Chemotherapy;

Variables	Overall (n = 158)	Responders (TRG = 1a/1b, n = 65)	Non-responders (TRG = 2 / 3, n = 93)	χ2/t/Z value	*P* value
CEA(ng/ml)				0.30	0.58
-	103 (65.19)	44 (67.69)	59 (63.44)		
+	55 (34.81)	21 (32.31)	34 (36.56)		
CA19-9(U/ml)				2.32	0.13
-	117 (74.05)	44 (67.69)	73 (78.49)		
+	41 (25.95)	21 (32.31)	20 (21.51)		
cT stage				5.99	0.05
2	10 (6.33)	7 (10.77)	3 (3.23)		
3	65 (41.14)	30 (46.15)	35 (37.63)		
4	83 (52.53)	28 (43.08)	55 (59.14)		
cN stage				0.97	0.81
0	14 (8.86)	7 (10.77)	7 (7.53)		
1	37 (23.42)	14 (21.54)	23 (24.73)		
2	67 (42.41)	29 (44.62)	38 (40.86)		
3	40 (25.32)	15 (23.08)	25 (26.88)		
NAC: Neoadjuvant Chemotherapy;					

Table 1b
Comparison of baseline imaging characteristics between the NAT response group and the no-response group

Variables	Overall (n = 158)	Responders (TRG = 1a/1b, n = 65)	Non-responders (TRG = 2 / 3, n = 93)	χ2/t/Z value	*P* value
Imaging morphological characteristics					
ctSI				3.96	0.05
Negative	75 (47.47)	37 (56.92)	38 (40.86)		
Positive	83 (52.53)	28 (43.08)	55 (59.14)		
ctEMVI				30.90	< 0.001
Negative	68 (43.04)	45 (69.23)	23 (24.73)		
Positive	90 (56.96)	20 (30.77)	70 (75.27)		
ctOPM				14.27	< 0.001
Negative	110 (69.62)	56 (86.15)	54 (58.06)		
Positive	48 (30.38)	9 (13.85)	39 (41.94)		
ctLVI				20.02	< 0.001
Negative	41 (25.95)	29 (44.62)	12 (12.90)		
Positive	117 (74.05)	36 (55.38)	81 (87.10)		
Spectral CT and derived imaging parameters					
Arterial phase					
ICAP	13.10(10.49,16.21)	14.47 (12.75, 19.54)	12.14 (9.51, 14.74)	-3.93	< 0.001
nICAP	0.11 (0.08, 0.14)	0.12 (0.09, 0.15)	0.10 (0.07, 0.13)	-3.42	< 0.001
40kevAP	141.44(113.27,176.16)	144.28 (113.08, 172.13)	137.16 (113.85, 176.88)	-0.21	0.84
70kevAP	64.58 (53.39, 76.64)	67.85 (55.32, 75.75)	62.54 (53.05, 77.52)	-0.94	0.35
λAP	2.59 (2.05, 3.34)	2.58 (1.95, 3.34)	2.60 (2.14, 3.34)	-0.30	0.77

Variables	Overall (n = 158)	Responders (TRG = 1a/1b, n = 65)	Non-responders (TRG = 2 / 3, n = 93)	χ2/t/Z value	*P* value
Imaging morphological characteristics					
Venous phase					
ICVP	16.87 (14.22, 19.86)	18.00 (15.41, 21.73)	15.86 (13.86, 18.34)	-3.12	0.002
nICVP	0.41 (0.35, 0.50)	0.45 (0.37, 0.58)	0.39 (0.35, 0.47)	-2.65	0.008
40kevVP	170.20 ± 40.24	171.57 ± 43.77	169.25 ± 37.79	0.36	0.72
70kevVP	72.73 ± 14.79	75.32 ± 15.77	70.92 ± 13.86	1.85	0.07
λVP	3.26 (2.73, 3.65)	3.31 (2.68, 3.69)	3.26 (2.80, 3.64)	-0.00	0.10
Delay phase					
ICDP	16.38 ± 4.39	16.34 ± 4.64	16.41 ± 4.22	-0.10	0.92
nICDP	0.60 ± 0.15	0.60 ± 0.16	0.60 ± 0.15	0.00	0.10
40kevDP	169.74 ± 38.25	165.62 ± 37.84	172.61 ± 38.47	-1.13	0.26
70kevDP	73.22 ± 13.99	73.08 ± 13.44	73.32 ± 14.43	-0.11	0.92
λDP	3.24 (2.89, 3.73)	3.24 (2.72, 3.65)	3.27 (2.92, 3.77)	-0.78	0.44
Post-processing parameters					
AEF	0.82 (0.69, 1.07)	1.00 (0.80, 1.17)	0.77 (0.61, 0.86)	-4.57	< 0.001
ECV	0.36 ± 0.09	0.36 ± 0.09	0.36 ± 0.09	0.60	0.55

Independent predictors of NAT response

In the multivariate logistic regression analysis, arterial phase iodine concentration (ICAP) was excluded due to multicollinearity (VIF > 5)(**Supplementary Table S6**). The results indicate that NLR (odds ratio [OR] = 1.680, 95% confidence interval [CI] 1.160–2.567; *p* = 0.01), ICVP (OR = 0.853, 95% CI 0.731–0.987; *p* = 0.04), AEF (OR = 0.195, 95% CI 0.044–0.812; *p* = 0.03), ctEMVI (OR = 6.473, 95% CI 2.450–18.744; *p* <

0.001), ctOPM (OR = 3.103, 95% CI 1.140–9.129; *p* = 0.03), and ctLVI (OR = 3.307, 95% CI 1.190–9.647; *p* = 0.02) all independently correlated with the response status to NAT(Table 2).

Table 2
Multivariable logistic regression analysis for predictors of response to NAT

Variable	**OR**	**95%CI**	***P***
NLR	1.680	1.160–2.567	0.01
nICAP	0.247	0.529-441.165	0.73
ICVP	0.853	0.731–0.987	0.04
nICVP	24.094	0.118-5770.270	0.24
AEF	0.195	0.044–0.812	0.03
ctSI	0.354	0.111–1.007	0.06
ctEMVI	6.473	2.450-18.744	<0.001
ctOPM	3.103	1.140–9.129	0.03
ctLVI	3.307	1.190–9.647	0.02

Considering that the range of nICAP and nICVP is between 0 and 1, for each 0.1 unit increase, the OR for nICAP is 0.869 (95% CI: 0.938–1.838, p = 0.73); the OR for nICVP is 1.375 (95% CI: 0.808–2.377, p = 0.24).

Construction of ctSLEP score and comparison of predictive model performance

Eight predictive models (Models 1–8) were developed by integrating spectral CT parameters, NLR, and either a single invasive imaging sign or a composite ctSLEP score. Model discrimination was assessed using the area under the receiver operating characteristic curve (AUC) (Fig. 3a-b). Among single-feature models, Model 2 achieved high AUCs in both the training (0.847) and validation (0.777) sets. In composite models, Model 7 slightly outperformed Model 6 (AUC 0.864 vs. 0.853), while Model 8 showed a higher training AUC than Model 7 (0.878) but was still lower than Model 5 (0.880). Based on comprehensive evaluation of AUC, calibration, and decision curve analysis, Model 5 was selected as the final model, demonstrating strong consistency and clinical value (Fig. 4a–c, Table 3 and **Supplementary Table S7**). Feature importance was quantified using Shapley Additive Explanations (SHAP) (Fig. 4d), and the final model was visualized as a nomogram (Fig. 4e).

Table 3
Predictive performance of eight candidate models for NAT response in the training and internal validation sets

Models	Sets	AUC	95%CI	P*	Cut-off value
Model 1	Training	0.770	0.682–0.858	0.40	0.683
	Testing	0.696	0.539–0.854		
Model 2	Training	0.847	0.774–0.920	0.40	0.670
	Testing	0.777	0.641–0.913		
Model 3	Training	0.808	0.729–0.886	0.30	0.715
	Testing	0.716	0.563–0.869		
Model 4	Training	0.825	0.747–0.903	0.30	0.721
	Testing	0.734	0.589–0.878		
Model 5	Training	0.880	0.818–0.941	0.20	0.722
	Testing	0.784	0.647–0.921		
Model 6	Training	0.853	0.783–0.923	0.10	0.571
	Testing	0.727	0.574–0.880		
Model 7	Training	0.864	0.799–0.930	0.10	0.524
	Testing	0.725	0.573–0.877		
Model 8	Training	0.878	0.815–0.940	0.20	0.537
	Testing	0.768	0.629–0.907		

** The P-value was calculated using the log-rank test.*

To comprehensively assess tumor invasiveness and improve score interpretability, we evaluated several strategies to construct the composite ctSLEP score:

(1) Weighted-index method: ctSLEP_weighted = -1.2160 − 0.9795·ctSI + 1.8200·ctEMVI + 1.1140·ctOPM + 1.1237·ctLVI,where the weights were derived from the β coefficients estimated using five-fold cross-validation.
(2) Additive-score method:ctSLEP_add = ctSI + ctEMVI + ctOPM + ctLVI.
(3) PCA-based score (principal component analysis): PCA was performed on the four invasive imaging sign scores, and principal components were retained according to the proportion of variance explained to derive a composite score.
All-features method:ctSI, ctEMVI, ctOPM, and ctLVI were entered simultaneously.

Using either a single invasive imaging sign (ctSI/ctEMVI/ctOPM/ctLVI) or one of the four ctSLEP construction strategies (Weighted-index/Additive/PCA/All), we combined the resulting imaging score with NLR, nICAP, ICVP, nICVP, and AEF to develop eight candidate models (Models 1–8): Model 1: ctSI + NLR, nICAP, ICVP, nICVP, and AEF; Model 2: ctEMVI + NLR, nICAP, ICVP, nICVP, and AEF; Model 3: ctOPM + NLR, nICAP, ICVP, nICVP, and AEF; Model 4: ctLVI + NLR, nICAP, ICVP, nICVP, and AEF; Model 5: ctSLEP score based on Weighted-index + NLR, nICAP, ICVP, nICVP, and AEF; Model 6: ctSLEP score based on Additive + NLR, nICAP, ICVP, nICVP, and AEF; Model 7: ctSLEP score based on PCA + NLR, nICAP, ICVP, nICVP, and AEF; Model 8: ctSI, ctEMVI,ctOPM and ctLVI + NLR, nICAP, ICVP, nICVP, and AEF.

Assessing the relationship between invasive imaging scores and recurrence-free survival

During follow-up (range, 3.1–58.1 months; median, 12.2 months), postoperative disease progression occurred in 35 patients (22.2%)(**Supplementary Figure S3**). Kaplan–Meier analyses showed significantly worse RFS in patients with ctEMVI-, ctLVI-, or ctOPM-positive status and in those with a higher ctSLEP score (log-rank $p < 0.05$; Fig. 5a–e). After confirming the proportional hazards assumption, multivariable Cox proportional hazards regression demonstrated that each 1-unit increase in the weighted ctSLEP index was associated with an increased risk of relapse or metastasis (hazard ratio [HR] = 2.63, 95% CI 1.86–3.72; $p < 0.001$). The weighted index provided the highest concordance among the evaluated imaging features (C-index = 0.825; **Supplementary Table S8**).

Discussion

In this study, we developed a novel ctSLEP score and integrated it with spectral CT parameters and systemic inflammatory biomarkers to construct a multidimensional predictive model. The optimal Model 5 achieved an integrated representation of morphological, functional, and biological imaging dimensions. This model exhibited excellent discriminative performance for preoperative prediction of NAT response in patients with LAGC (AUC = 0.880, 95% CI: 0.818–0.941) and showed a strong association with RFS. These findings indicate that the ctSLEP-based model represents a promising noninvasive imaging biomarker for early identification of patients likely to benefit from NAT, thereby supporting individualized treatment planning and prognostic assessment.

In Model 5, the weighted ctSLEP index, which showed the greatest contribution, is composed of four CT-detected imaging features that reflect tumor invasiveness and metastatic potential, revealing the complex heterogeneity of the tumor microenvironment. Among them, the ctEMVI feature indicates the early stage of hematogenous metastasis and is closely associated with treatment resistance and poor prognosis[8, 10]. ctLVI, characterized by flocculent shadows between the tumor and lymph nodes, suggests the potential risk of lymphatic metastasis[13]. The high invasiveness of GC may be closely linked to VEGF overexpression, which drives angiogenesis, endothelial cell migration, and distant metastasis[21–23]. For instance, Gao et al[10]demonstrated that gene features associated with ctEMVI accelerate hematogenous metastasis by modulating tumor angiogenesis and collagen remodeling, with

significantly elevated VEGF-A and FLT1 gene expression in EMVI-positive patients. This finding is consistent with Kim et al.[24] reported that even in the absence of clear metastatic lesions on imaging, EMVI positivity still indicates the risk of micrometastasis[21]. The ctSI sign suggests that the tumor may infiltrate adjacent organs via invasive growth, substantially increasing the risk of peritoneal metastasis[25, 26]. ctOPM serves as an early indicator of PM. Peritoneal metastasis driven by cancer-associated fibroblasts (CAFs) may lead to the appearance of fibrous string-like shadows on CT[27]. Free-floating cancer cells in the peritoneal cavity specifically deposit in lymphatic openings and proliferate in the subserosal lymphatic space, resulting in peritoneal proliferation and increased blood supply, which may explain the mechanism behind the S-GGO appearance on CT[28].

Spectral CT parameters, as functional markers, further complement the invasive morphological features. Specifically, IC reflects tumor blood perfusion at a particular stage[29]. Lower IC values indicate poor tumor blood supply and oxygenation, leading to tumor hypoxia, which drives genetic instability and may induce drug resistance, thereby increasing the risk of invasion and metastasis[16, 30]. This finding aligns with the observation in this study that non-responders to NAT exhibited lower IC compared to responders, consistent with previous studies[31, 32]. Furthermore, we found that ICVP is the second most contributing factor in Model 5, likely due to its reflection of iodine distribution in tumor vascular regions and its stronger correlation with tumor microvascular density (MVD)[16]. Our study also found that IC-derived AEF was significantly and positively correlated with the NAT response, a finding also reported by Li et al[33]. This may be attributed to the increased AEF being associated with enhanced tumor vascular permeability, thereby facilitating the penetration of chemotherapeutic agents. Additionally, NLR, reflecting systemic inflammation, has been shown to be a significant predictor, and in this study, the NLR was lower in responders compared to non-responders ($p < 0.05$), aligning with the findings of Wang et al[34].

Despite the strengths of this study, there are several limitations. First, it is a single-center retrospective study, and further validation in a multi-center, large-scale cohort is necessary. Second, while we employed rigorous imaging assessment methods, the inherent subjectivity of image interpretation remains a concern. Future studies should focus on standardizing image interpretation, particularly through the development of semi-automated and automated measurement tools, to minimize human variability. Additionally, this study used only baseline imaging data, and future research may benefit from incorporating longitudinal imaging data. Finally, this study was based on spectral CT scanners from a specific manufacturer, which may limit the generalizability of the results to other platforms.

Conclusion

The integrated model combining spectral CT parameters with the ctSLEP score enables accurate, noninvasive prediction of neoadjuvant therapy response and relapse risk in patients with locally advanced gastric cancer by capturing tumor invasiveness and functional heterogeneity. This

multiparametric model offers a clinically applicable tool for individualized treatment planning and prognostic evaluation, holding potential to improve therapeutic decision-making in clinical practice.

Abbreviations

AEF: arterial enhancement fraction

AJCC: American Joint Committee on Cancer

AP: arterial phase

AUC: area under the receiver operating characteristic curve

BMI: body mass index

CA19-9: carbohydrate antigen 19-9

CAF: cancer-associated fibroblast

CEA: carcinoembryonic antigen

CI: confidence interval

CT: computed tomography

ctEMVI: CT-detected extramural vascular invasion

ctLVI: CT-detected lymphovascular invasion

ctOPM: CT-detected occult peritoneal metastasis

ctSI: CT-detected serosal invasion

ctSLEP: CT-based serosal invasion, lymphovascular invasion, extramural vascular invasion, and occult peritoneal metastasis score

DCA: decision curve analysis

DP: delayed phase

ECV: extracellular volume fraction

EMVI: extramural vascular invasion

GC: gastric cancer

HCT: hematocrit

HR: hazard ratio

IC: iodine concentration

ICAP: iodine concentration in the arterial phase

ICDP: iodine concentration in the delayed phase

ICVP: iodine concentration in the venous phase

ICC: intraclass correlation coefficient

IQR: interquartile range

IRB: Institutional Review Board

LAGC: locally advanced gastric cancer

LMR: lymphocyte-to-monocyte ratio

LVI: lymphovascular invasion

MVD: microvascular density

NAC: neoadjuvant chemotherapy

NAT: neoadjuvant therapy

nIC: normalized iodine concentration

nICAP: normalized iodine concentration in the arterial phase

nICDP: normalized iodine concentration in the delayed phase

nICVP: normalized iodine concentration in the venous phase

NLR: neutrophil-to-lymphocyte ratio

NPV: negative predictive value

OR: odds ratio

PCA: principal component analysis

PM: peritoneal metastasis

PPV: positive predictive value

RFS: relapse-free survival

ROI: region of interest

SD: standard deviation

SHAP: Shapley Additive Explanations

SI: serosal invasion

TRG: tumor regression grade

UICC: Union for International Cancer Control

VEGF: vascular endothelial growth factor

VIF: variance inflation factor

VP: venous phase

λHU: slope of the spectral attenuation curve

κ: Cohen's kappa

Declarations

Ethics approval and consent to participate:

This retrospective study was approved by the Institutional Medical Ethics Committee of the Second Hospital of Lanzhou University (Approval No. 2025A-1258). The requirement for written informed consent to participate was waived by the Institutional Medical Ethics Committee of the Second Hospital of Lanzhou University due to the retrospective nature of the study. The study was conducted in accordance with the Declaration of Helsinki.

Consent for publication:

Not applicable.

Competing interests:

The authors declare that they have no competing interests.

Funding:

From Major Project of the Gansu Province Joint Research Fund(24JRRA921), Youth Science and Technology Talent Innovation Project of Lanzhou (2023-2-44).

Author Contribution

Guarantors of integrity of entire study: P.Y.; study concepts/study design or data acquisition or data analysis/interpretation: all authors; approval of final version of submitted manuscript: all authors; agrees to ensure any questions related to the work are appropriately resolved: all authors; manuscript drafting: P.Y.; statistical analysis: P.Y., G.X. , M.L. and T.Z.R; manuscript editing: Z.W.J., R.T.Z. and C.Q.Q. All authors read and approved the final manuscript.

Acknowledgements:

Not applicable.

Data Availability

The datasets generated or analyzed during this study are available from the corresponding author upon reasonable request.

References

1. Bray F, Laversanne M, Sung H, et al. Global cancer statistics 2022: GLOBOCAN estimates of incidence and mortality worldwide for 36 cancers in 185 countries. CA Cancer J Clin. 2024;74:229–63.
2. (2025) Correction to Cancer treatment and survivorship statistics, 2025. CA Cancer J Clin 75:683.
3. Ajani JA, D'Amico TA, Bentrem DJ, et al. Gastric Cancer, Version 2.2025, NCCN Clinical Practice Guidelines In Oncology. J Natl Compr Canc Netw. 2025;23:169–91.
4. Wang FH, Zhang XT, Tang L, et al. The Chinese Society of Clinical Oncology (CSCO): Clinical guidelines for the diagnosis and treatment of gastric cancer, 2023. Cancer Commun (Lond). 2024;44:127–72.
5. Coccolini F, Nardi M, Montori G, et al. Neoadjuvant chemotherapy in advanced gastric and esophago-gastric cancer. Meta-analysis of randomized trials. Int J Surg. 2018;51:120–7.
6. Sylvie L, Susanne B, Katja O. Prediction of response and prognosis by a score including only pretherapeutic parameters in 410 neoadjuvant treated gastric cancer patients. Recent Results Cancer Res. 2012;196:269–89.
7. Westerhoff M, Osecky M, Langer R. Varying practices in tumor regression grading of gastrointestinal carcinomas after neoadjuvant therapy: results of an international survey. Mod Pathol. 2020;33:676–

89.

8. Yang YT, Dong SY, Zhao J, Wang WT, Zeng MS, Rao SX. CT-detected extramural venous invasion is corelated with presence of lymph node metastasis and progression-free survival in gastric cancer. Br J Radiol. 2020;93:20200673.
9. Yang L, Sun J, Yu X, et al. Diagnosis of Serosal Invasion in Gastric Adenocarcinoma by Dual-Energy CT Radiomics: Focusing on Localized Gastric Wall and Peritumoral Radiomics Features. Front Oncol. 2022;12:848425.
10. Gao B, Feng C, Chai F, et al. CT-detected extramural venous invasion-related gene signature for the overall survival prediction in patients with gastric cancer. Cancer Med. 2021;10:7816–30.
11. Liu S, He J, Liu S, et al. Radiomics analysis using contrast-enhanced CT for preoperative prediction of occult peritoneal metastasis in advanced gastric cancer. Eur Radiol. 2020;30:239–46.
12. Li Q, Feng QX, Qi L, et al. Prognostic aspects of lymphovascular invasion in localized gastric cancer: new insights into the radiomics and deep transfer learning from contrast-enhanced CT imaging. Abdom Radiol (NY). 2022;47:496–507.
13. Li Q, Jiang Z, Zhu Y, et al. CT-based scores for extramural vascular invasion and occult peritoneal metastasis correlate with gastric cancer survival. Eur Radiol. 2025;35:5733–47.
14. Zhao L, Zhou W, Fu Y, et al. Diagnostic value of one-stop CT energy spectrum and perfusion for angiogenesis in colon and rectum cancer. BMC Med Imaging. 2024;24:116.
15. Adam SZ, Rabinowich A, Kessner R, Blachar A. Spectral CT of the abdomen: Where are we now? Insights Imaging. 2021;12:138.
16. Chen XH, Ren K, Liang P, Chai YR, Chen KS, Gao JB. Spectral computed tomography in advanced gastric cancer: Can iodine concentration non-invasively assess angiogenesis? World J Gastroenterol. 2017;23:1666–75.
17. Lin X, Xu S, Wang Y, et al. Sequential dual-energy CT for longitudinal assessment of pathologic response to neoadjuvant immuno-chemotherapy in locally advanced gastric cancer. Eur Radiol. 2025;35:6469–81.
18. Chen Y, Xi W, Yao W, et al. Dual-Energy Computed Tomography-Based Radiomics to Predict Peritoneal Metastasis in Gastric Cancer. Front Oncol. 2021;11:659981.
19. Ge HT, Chen JW, Wang LL, et al. Preoperative prediction of lymphovascular and perineural invasion in gastric cancer using spectral computed tomography imaging and machine learning. World J Gastroenterol. 2024;30:542–55.
20. Li J, Chen X, Xu S, et al. Predicting pathologic response to neoadjuvant chemotherapy in locally advanced gastric cancer: The establishment of a spectral CT-based nomogram from prospective datasets. Eur J Surg Oncol. 2024;50:108020.
21. Oommen S, Gupta SK, Vlahakis NE. Vascular endothelial growth factor A (VEGF-A) induces endothelial and cancer cell migration through direct binding to integrin {alpha}9{beta}1: identification of a specific {alpha}9{beta}1 binding site. J Biol Chem. 2011;286:1083–92.

22. Maehara Y, Kabashima A, Koga T, et al. Vascular invasion and potential for tumor angiogenesis and metastasis in gastric carcinoma. Surgery. 2000;128:408–16.
23. Zeng YJ, Zhang CD, Dai DQ. Impact of lymph node micrometastasis on gastric carcinoma prognosis: a meta-analysis. World J Gastroenterol. 2015;21:1628–35.
24. Kim TU, Kim S, Lee NK, et al. Prognostic Value of Computed Tomography-Detected Extramural Venous Invasion to Predict Disease-Free Survival in Patients With Gastric Cancer. J Comput Assist Tomogr. 2017;41:430–6.
25. Liu Y, Yuan M, Zhao Z, et al. A quantitative model using multi-parameters in dual-energy CT to preoperatively predict serosal invasion in locally advanced gastric cancer. Insights Imaging. 2024;15:264.
26. Chen D, Liu Z, Liu W, et al. Predicting postoperative peritoneal metastasis in gastric cancer with serosal invasion using a collagen nomogram. Nat Commun. 2021;12:179.
27. Yan Y, Wang LF, Wang RF. Role of cancer-associated fibroblasts in invasion and metastasis of gastric cancer. World J Gastroenterol. 2015;21:9717–26.
28. Al-Shammaa HA, Li Y, Yonemura Y. Current status and future strategies of cytoreductive surgery plus intraperitoneal hyperthermic chemotherapy for peritoneal carcinomatosis. World J Gastroenterol. 2008;14:1159–66.
29. Deniffel D, Sauter A, Fingerle A, Rummeny EJ, Makowski MR, Pfeiffer D. Improved differentiation between primary lung cancer and pulmonary metastasis by combining dual-energy CT-derived biomarkers with conventional CT attenuation. Eur Radiol. 2021;31:1002–10.
30. Kumareswaran R, Ludkovski O, Meng A, Sykes J, Pintilie M, Bristow RG. Chronic hypoxia compromises repair of DNA double-strand breaks to drive genetic instability. J Cell Sci. 2012;125:189–99.
31. Deng J, Zhang W, Xu M, et al. Value of spectral CT parameters in predicting the efficacy of neoadjuvant chemotherapy for gastric cancer. Clin Radiol. 2024;79:51–9.
32. Lin Y, Lan Y, Zheng Y, Ma M. Dual-energy CT for evaluating the tumor regression grade of gastric cancer after neoadjuvant chemotherapy. Eur Radiol. 2025;35:5748–59.
33. Li M, Cui Y, Yan Y, et al. Dual energy CT-derived quantitative parameters and hematological characteristics predict pathological complete response in neoadjuvant chemoradiotherapy esophageal squamous cell carcinoma patients. BMC Gastroenterol. 2025;25:357.
34. Wang J, Zhu Y, Li Q, et al. Spectral CT-based nomogram for evaluation of neoadjuvant chemotherapy response in esophageal squamous cell carcinoma. Eur Radiol. 2025;35:3800–11.

Figures

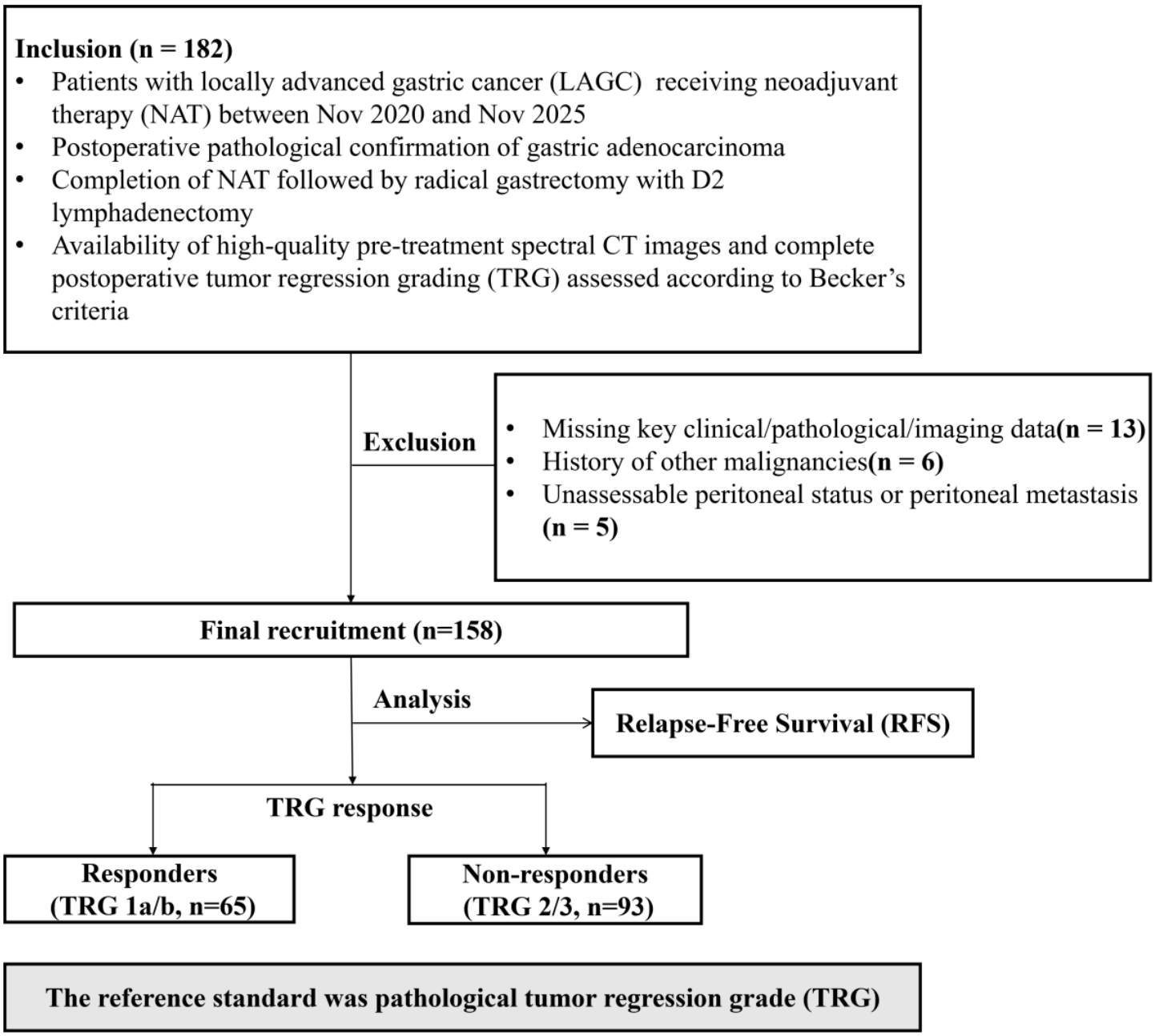


Figure 1

Diagram showing the patient inclusion and exclusion process

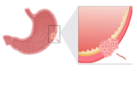
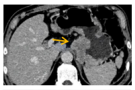
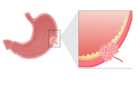
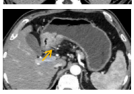
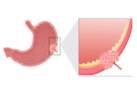
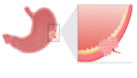
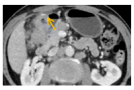
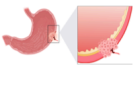
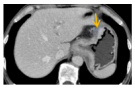
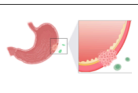
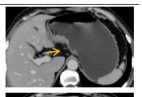
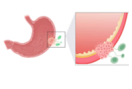
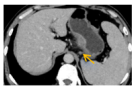
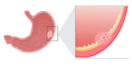
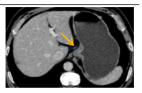
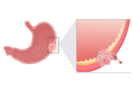
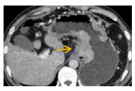
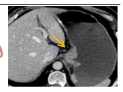
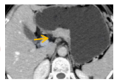
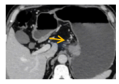
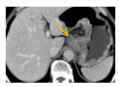
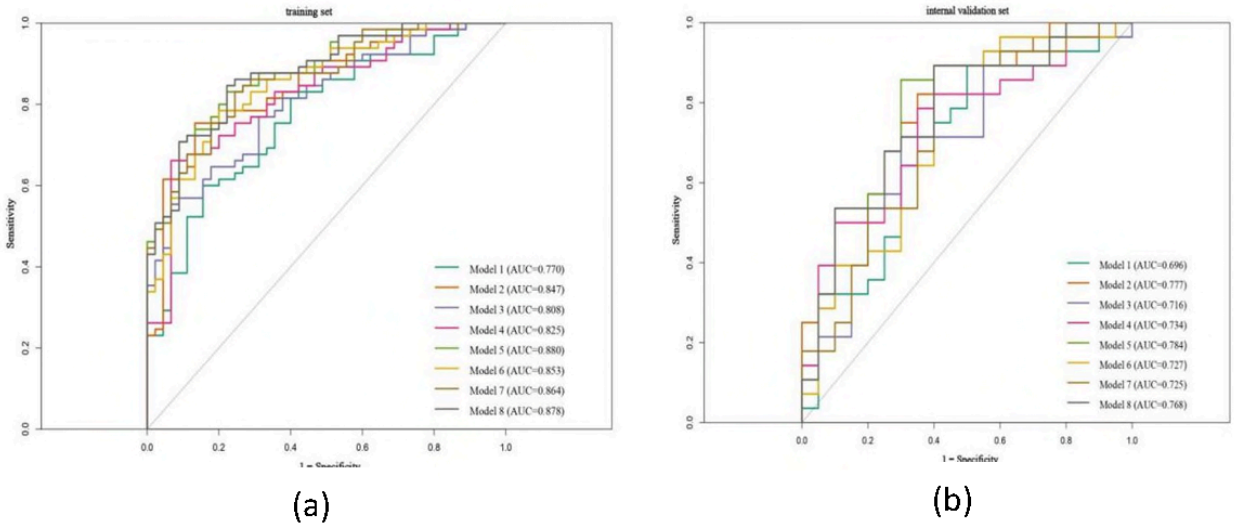
Score	Imaging Criteria	Properties	Illustration	CT Schematic Diagram
ctEMVI (Extraluminal Venous Invasion) Scoring Criteria				
0	The tumor does not show nodular penetration through the gastric wall, and no vessels are present in the tumor area.	(-)		
1	The tumor penetrates the gastric wall, but no blood vessels are connected to the tumor outside the gastric wall.			
2	Blood vessels run naturally outside the tumor invasion area, without intraluminal abnormal soft tissue and without vascular dilatation.			
3	The tumor penetrates the gastric wall, and abnormal soft-tissue density is observed in the lumen of extramural vessels, without significant vessel thickening and with smooth vessel margins.			
4	The tumor penetrates the gastric wall, with intraluminal abnormal soft-tissue density and mild vascular thickening (≤1.5 times the normal diameter).	(+)		
5	The tumor penetrates the gastric wall, with intraluminal abnormal soft-tissue density, marked vascular thickening (>1.5 times the normal diameter), and irregular vessel margins.			
(-): Negative, (+): Positive				
ctLVI (Extraluminal Lymphatic Vessel Invasion) Scoring Criteria				
0	The tumor does not penetrate the gastric wall, or penetrates the wall without flocculent shadow connected to lymphatic vessels in the invasive area.	(-)		
1	The tumor penetrates the gastric wall, and flocculent shadows extend toward adjacent lymph nodes, which are visible around the lesion.	(+)		
ctSI(CT-based Serosal Invasion) Scoring Criteria				
0	The outer layer of the gastric wall remains smooth and intact, with a clear perigastric fat plane.	(-)		
1	Irregular or nodular thickening of the outer gastric wall with blurring or obliteration of the perigastric fat plane, without definite extramural vascular or lymphatic invasion.	(+)		
ctOPM(Omental/Peritoneal Metastasis) Scoring Criteria				
Score	**Free Peritoneum**	**Peritoneum Covering Organs or Tissues**	**Properties**	**Illustration** / **CT Schematic Diagram**
0	No abnormal findings.	No abnormal linear structures.	(-)	 
1	Slight and homogeneous increase in fat density, appearing as small ground-glass opacity (S-GGO).	Slightly thickened linear structure.		 
2	Heterogeneous increase in density with patchy or intense S-GGO.	Obviously thickened linear structure with enhancement.		 
3	Marked heterogeneous density increase with intense S-GGO, multiple strands or curled signs, or blurred small nodules.	Obviously thickened linear structure with enhancement and tiny nodules or a small amount of ascites.	(+)	 

Figure 2

CT Invasive Imaging Signs Scoring Criteria



1

Figure 3

a-b Discrimination of eight predictive models in the training and internal validation sets. (a) Training set; (b) internal validation set

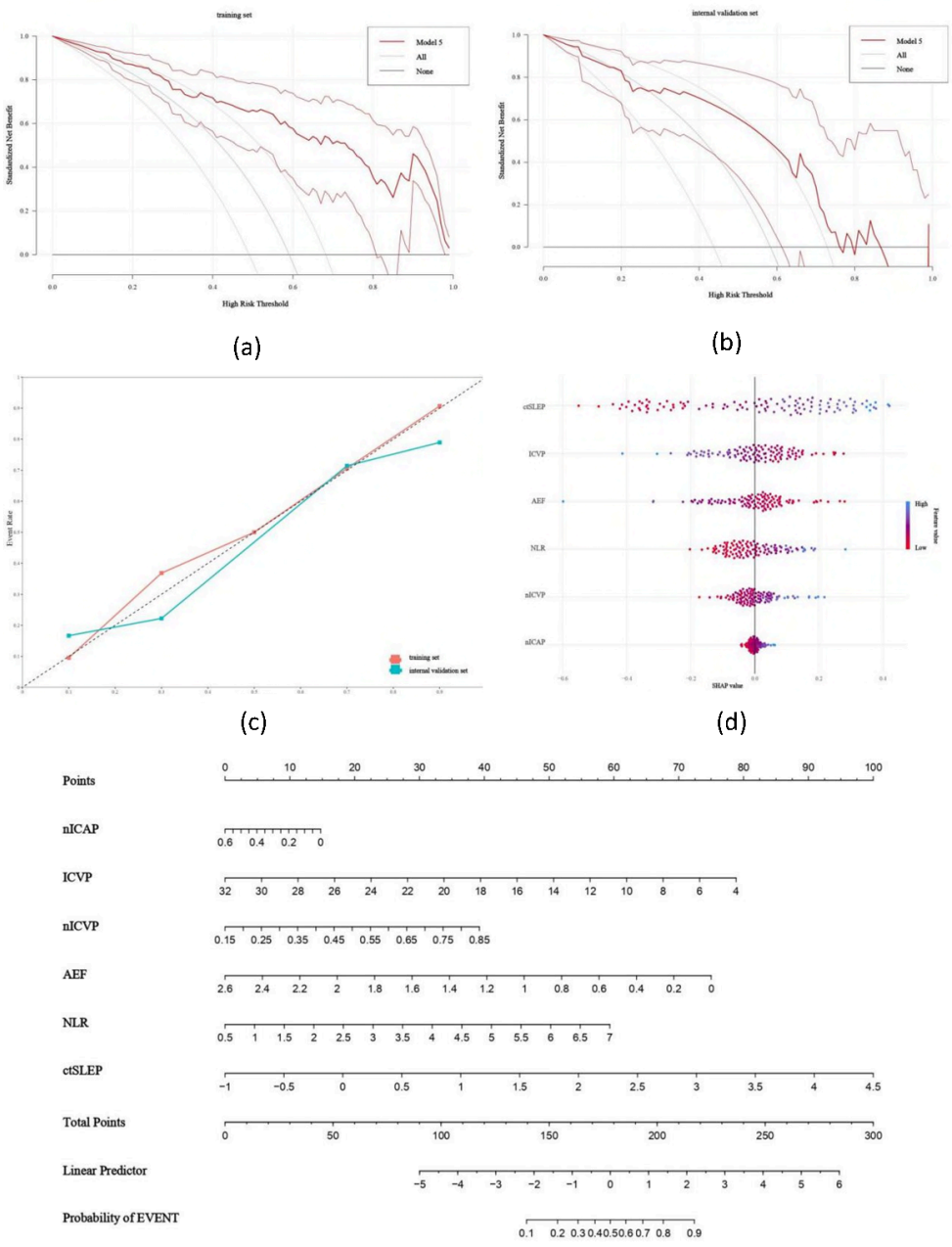


Figure 4

a-e Performance, interpretability, and visualization of the optimal model. (a–b) Decision curve analysis (DCA) of Model 5 in the training and internal validation sets. (c) Calibration curves of Model 5 in the training and internal validation sets. (d) Shapley Additive Explanations (SHAP) summary plot showing feature importance in Model 5. (e) Nomogram for individualized prediction of NAT response based on Model 5

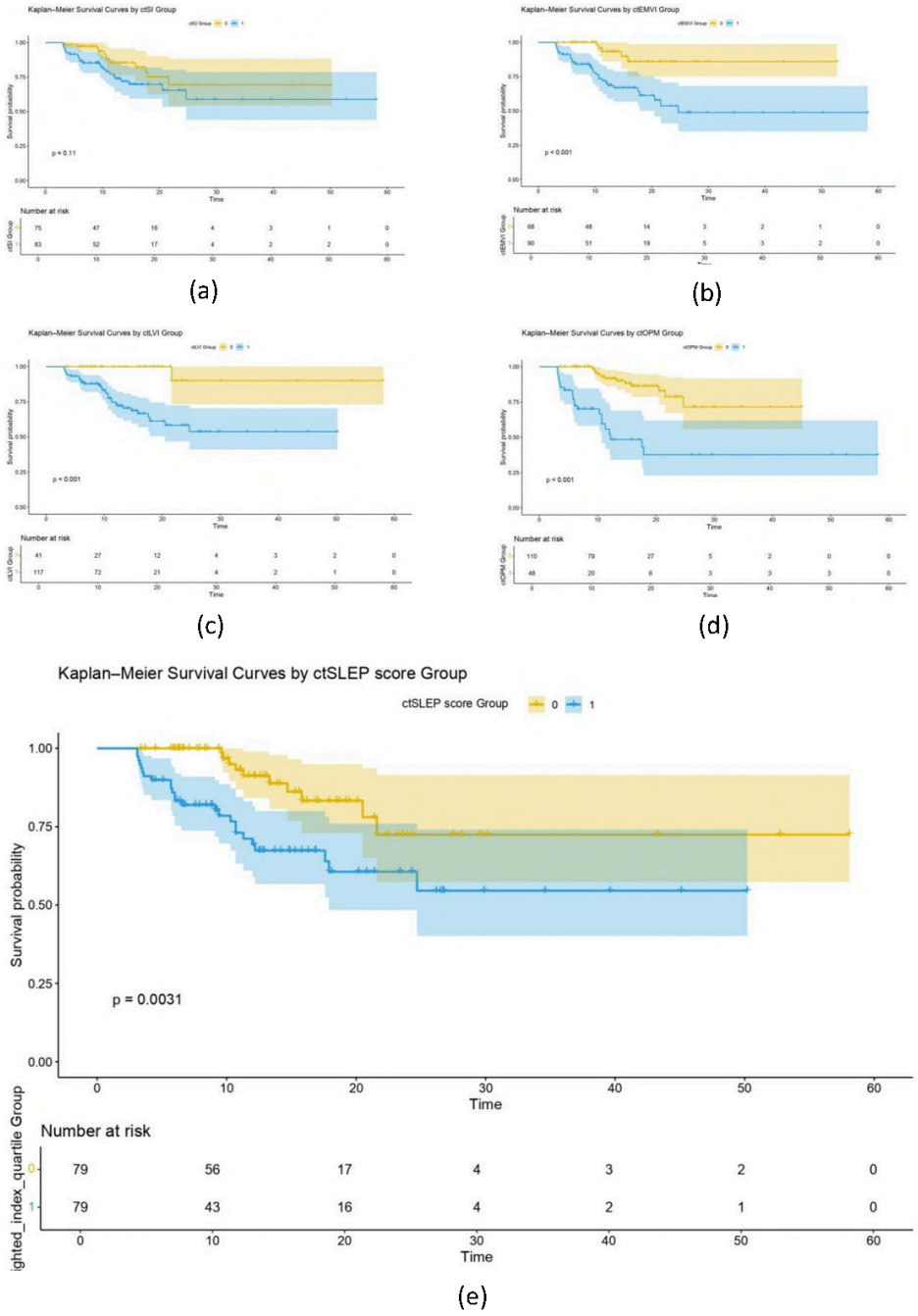


Figure 5

a-e Kaplan–Meier curves of relapse-free survival (RFS) stratified by (a) ctSI, (b) ctEMVI, (c) ctLVI, (d) ctOPM, and (e) ctSLEP. The ctSLEP score was dichotomized at the median (0 vs 1)

Supplementary Files

This is a list of supplementary files associated with this preprint. Click to download.

- SupplementaryMaterialBMC.docx